COMMUNICATIONS EARTH&ENVIRONMENT

ARTICLE

https://doi.org/10.1038/s43247-020-00051-0 OPEN

Magmatic volatiles episodically flush oceanic hydrothermal systems as recorded by zoned epidote

Stephen Fox[1]✉, Yaron Katzir[1], Wolfgang Bach[2], Lucy Schlicht[2] & Justin Glessner[3]

Circulation of seawater at oceanic spreading centers extracts heat, drives rock alteration, and transports leached metals to shallower levels of the crust, where they may precipitate and form ore deposits. Crystallization of the lower crust, may exsolve and introduce magmatic volatiles into the seawater-dominant system. However, the role of magmatic volatiles added to the hydrothermal system, including pathways of these fluids are lesser known. Here we present coupled in-situ strontium isotope and rare earth element data of distinct domains in epidote, a common hydrothermal mineral throughout the Troodos ophiolite, to track magmatic fluid input and flow. Epidote crystal domains characterize three distinct strontium isotope-rare earth element signatures—suggesting sequential growth from magma-derived fluids (0.704, negative europium anomalies), rock-buffered fluids (0.7055, positive europium anomalies) and seawater-derived fluids (0.7065, negative cerium anomalies). Epidote records episodic fluxing of magmatic fluids from plagiogranites, through epidosites in the upflow zone and into metal ore deposits.

[1] Department of Earth and Environmental Sciences, Ben Gurion University of the Negev, Be'er Sheva 84105, Israel. [2] Faculty of Geosciences, University of Bremen, Klagenfurter Straße 2-4, 28359 Bremen, Germany. [3] Interdisciplinary Center for Plasma Mass Spectrometry, University of California, Davis, Earth and Physical Sciences Bldg., Davis, CA 95616, USA. ✉email: sthephen@post.bgu.ac.il

Since the first discovery of submarine hydrothermal vents (black-smokers), at the East Pacific Rise in the late 1970's[1], hydrothermal mineralization has been found abundantly along earth oceanic spreading centers[2]. The modern fluid venting from seafloor hydrothermal fields is predominantly seawater, heated by crystallizing magma emplaced in the lower crust[3]. Metals in ocean floor hydrothermal vents are thought to originate mostly from leaching of crustal rocks by heated seawater and subsequently precipitated as sulfides, when the discharging hydrothermal fluids mix with cold, metal–depleted seawater[4,5].

Magma-derived fluids added to the hydrothermal cell may contribute to the formation of ocean-floor sulfide deposits[6]. Favorable settings to test this hypothesis are Back Arc Basins (BAB) because volatile-rich felsic magmas, which concentrate many metals as they evolve, are much more common in back-arc settings than along mid-ocean ridges[7]. A particularly useful tool to identify the contribution of volatiles exsolved from silicic magmas to black smoker fluids are the set of Rare Earth Elements (REE). In Mid-Ocean Ridge (MOR) settings, the chondrite-normalized REE patterns of hydrothermal fluids are universally characterized by a strong positive Eu anomaly and LREE (light REE, La–Sm) enrichment[8,9]. This pattern stems from preferential complexing of the LREE and Eu^{2+} with chlorine, a major constituent of seawater[10]. However, recent discoveries of HREE (heavy REE, Gd–Lu) enrichment and weaker Eu anomalies in back-arc basin (BAB) fluids are explained by REE complexing with other ligands, such as fluoride and sulfate, under varying pH conditions[10,11]. The source of these fluids was inferred to be degassing of silicic magmas[12], but the exact identity of these silicic magmas has yet to be described. Furthermore, whether BAB-hosted complexing ligands only affect REE leaching from solid rocks or in fact transport the REE from the silicic magmas directly to the hydrothermal system is still unresolved.

The lower oceanic crust occurs at depths of ≥2 km below the seafloor, and hence the rootzones of the present-day oceanic hydrothermal systems are rarely accessible. Ancient oceanic crust exposed on-land in ophiolites is thus invaluable for assessing the role of magmatic fluids in oceanic hydrothermal systems and seafloor mineralization. In this respect, the Troodos ophiolite of Cyprus is a key exposure: (1) a well-preserved, intact crustal section is exposed, allowing the inspection of the ancient hydrothermal fingerprint in its full extent from rootzone through upflow zones to vents; (2) the most significant evidence for Volcanogenic Massive Sulfide (VMS) ores in ophiolites being ancient analogs of black smokers comes from Troodos[13,14]. Moreover, negative $\delta^{34}S$ values measured in sulfides from a few VMS deposits in Troodos suggest magmatic sulfur influx;[15] (3) Troodos is a supra-subduction zone (SSZ) ophiolite, representing BAB-type crust[16,17] and predictably contains conspicuous silicic intrusions, commonly known as plagiogranites.

The Troodos ophiolite (~92 Ma)[18,19] comprises mantle peridotites, overlain by a crustal section made of, from bottom to top (i) gabbros and minor plagiogranites, (ii) sheeted diabase dykes and (iii) lavas, mostly pillowed (Fig. 1). The VMS deposits of Cyprus, the type location for such worldwide Cyprus-style copper ore deposits, mainly occur near the top of the volcanic section of the ophiolite. Their geometry and alteration zonation are similar to hydrothermal vents at modern spreading centers[4,20]. The Cu, Zn, Pb and minor amounts of precious metals found in the VMS deposits are thought to derive from diabase dykes below the deposits by leaching along intensive hydrothermal upflow zones[21,22]. Mass balance calculations show that the base metal quota hosted in diabase is sufficient to supply the overlying VMS deposits, but requires fluid/rock interactions at substantially higher ratios than deduced for modern black smoker environments[5,23]. The leached zones are often seen as lenticular bodies rich in epidote-quartz ± chlorite assemblage in the center of dykes. In areas where the alteration is most destructive, pure epidote and quartz encompass the entire rock, known as epidosite[24]. These rocks were hypothesized to form where seawater-derived hydrothermal fluids are focused into narrow upflow pipes and epidotize the dike rocks at high water-to-rock ratios of 20 to 1000[23,25]. This model is petrologically implausible, because fluids that are multiply saturated with 5-6 greenschist facies minerals in the root zones are unlikely to dissolve all but two of those phases upon initial upwelling[26]. Thermodynamic modeling showed that epidosite formation requires some influx of hard mineral acids, like that seen in exsolved magmatic volatiles from siliceous magmas[26].

Fluid inclusions trapped in gabbros and plagiogranites of the Troodos ophiolite include dense brines of up to 60 wt.% NaCl, interpreted as derived from magmatic fluid sources[27]. The highly saline inclusion trails are not associated with low-salinity vapor phase inclusions, indicating derivation by direct exsolution from magma and not by phase separation of a seawater-derived fluid. Secondary epidote, especially abundant in Troodos plagiogranites, turns out to be excellent tracer of the evolution of fluids exsolved from magmas[28]. Hydrothermal epidote, precipitated in miarolites in plagiogranites, records REE-rich and Eu-depleted fluids exsolved from silicic magma early on, which gradually transform into the REE-depleted and Eu-enriched pattern prevalent throughout conventional seawater-derived sub-seafloor fluids. Thus, epidotization of plagiogranites is initially an autometasomatic process, whereby the rock is altered by supercritical fluids exsolving from the crystallizing magma rather than by seawater-derived fluids.

The question posed here is whether exsolved magmatic fluids are able to migrate through the plagiogranites into nearby and overlying rock suites, the sheeted diabase dykes, which are considered the root zone of the oceanic hydrothermal system[29–32]. Furthermore, do magmatic fluids enhance alteration of the middle and upper oceanic crust and contribute to mineralization on the ocean floor?

Results

Using Epidote to trace hydrothermal fluids. Epidote in the ocean crust is stable over a wide range of conditions[33] and potentially an excellent tracer mineral for the evolution of the sub-seafloor oceanic hydrothermal system. Epidote is also a strontium (Sr) and REE-bearing mineral, and since the possible end-members of circulating fluids, e.g. seawater and magmatic water, strongly differ in their REE contents and patterns as well as Sr isotope ratios, it makes a perfect recorder of relative contributions of these two fluid sources.

Textural types of epidote represent various stages of hydrothermal alteration of the Troodos crustal section: (a) epidote formed at the expense of plagioclase in the sheeted dykes as part of greenschist facies alteration; (b) hydrothermal epidote overgrowing and, in some cases, totally replacing type a; (c) precipitates in veins, miarolites and amygdules. Often all three textural types of epidote can occur in a single thin section. In-situ REE contents and Sr isotope ratios were measured by laser ablation inductively-coupled plasma mass spectrometry (LA-ICP-MS) techniques (quadrupole and multiple-collection sector MS, respectively) in epidote crystals from various crustal levels of the Troodos ophiolite. Sr isotope ratios of bulk epidote separates from rock matrices, veins and amygdules of the same samples chosen for in-situ analysis were measured by thermal ionization mass spectrometry (TIMS). The full REE—Sr isotope dataset and sampling locations are given in the supplementary section (Supplementary Data 1). Representative Sr isotope transects in

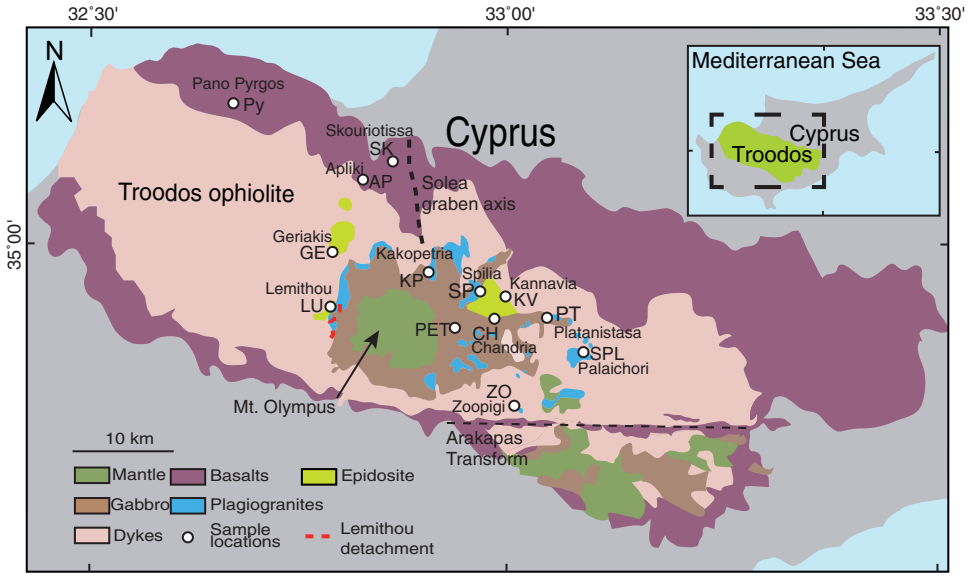

Fig. 1 Generalized geological map of Troodos Ophiolite, Cyprus. The major rock units of the oceanic lithosphere are shown; white circles are sampling sites. Black dashed line denotes the Solea graben, an ancient ocean ridge axis. Red dashed line denotes an oceanic detachment fault. Bright green areas are epidosite-rich domains[29]—highly altered diabase dykes interpreted as fossil hydrothermal upflow zones[31,32]. The map is based on the geological map of Cyprus produced by the Geological Survey Department, Cyprus.

zoned epidote and the corresponding REE patterns are shown on photomicrographs of rock thin sections in Fig. 2, 3; bulk epidote $^{87}Sr/^{86}Sr$ values are shown for comparison.

Combined REE patterns and $^{87}Sr/^{86}Sr$ ratios of epidote. Epidote, precipitated in amygdules from mineralized basalts at the Apliki copper mine (Fig. 1), is isotopically zoned: $^{87}Sr/^{86}Sr$ increases from 0.7049–0.7052 in the core (H) to 0.7057–0.7061 at the rim (MS) (following the blue arrow; Fig. 2a). However, an excursion to distinctly low value of 0.7044 in the core zone implies oscillatory isotope zonation. Whole grain epidotes separated from amygdules in this sample yielded a value of ~0.705 (black line), within the range of (H) values (Fig. 2b). REE patterns also reflect the distinct crystal zonation (Fig. 2c): flat patterns with minor light REE-enrichment (LREE) and positive Eu anomalies in H(1) domains and flat patterns with positive Eu and negative Ce anomalies in MS(1) domains. Amygdular epidotes from unmineralized basalts (Pyrgos, NW Cyprus) contain core regions that show an outwards increase in $^{87}Sr/^{86}Sr$ values from 0.7040–0.7044 to 0.7051–0.7053, which further increase towards the rim (0.7061) (Fig. 2d, e). The whole grain TIMS values, ~0.705, averages out the in-situ variability, while a laser ablation (LA) line analyzed across the amygdule yielded $^{87}Sr/^{86}Sr =$ 0.7057, slightly higher than the average values of the LA pits (Fig. 2e). The REE analysis along two radially-grown epidote crystals (Fig. 2c, f) yielded three distinct patterns: H(3)—flat patterns with positive Eu anomalies; MS(3)—LREE-depleted, positive Eu and negative Ce anomalies; and M(3)—heavy REE-enriched (HREE) with a negative Eu anomaly. Overall, in basalt amygdules, epidote (M) domains have lower Sr isotope ratios than (H) domains, while (MS) domains have higher ratios. Measured bulk epidote $^{87}Sr/^{86}Sr$ values average out these variations. Each of these Sr-isotope domains has a distinct REE pattern, and this Sr isotope-REE coupling is similar in basalts of different locations.

Epidotes analyzed from a fully epidotized region in the sheeted diabase dykes are shown in Fig. 2g. Sector and oscillatory zoned crystal cores are embayed and overgrown by thin euhedral rims. Sr isotope ratios in a large epidote (Fig. 2g, h; crystal #4) decrease from 0.7061–0.7065 at the rim, through 0.7050–0.7055 at the resorbed core edge, to inner core values of 0.7044–0.7046. Similar Sr-isotope values in the core and rim regions of a smaller adjacent epidote, 0.7042 and 0.7051, respectively (Fig. 2g, h; crystal #5) were calculated from a time-resolved LA line analysis (Fig. 2g). The coupled REE data of the core and rim region in this crystal correspond to (M)-like and (H)-like REE patterns (Fig. 2i). The REE patterns of (M) domains in epidosites are characteristically HREE > LREE with negative Eu anomalies; (H) domain REE patterns resemble those seen in the overlying basalts and diabases (Fig. 2i; Supplementary Data 1).

Sr isotope—REE coupling in epidotes from miarolites and epidotized regions in plagiogranites are similar to that observed in epidosite matrix and amygdules in shallower rocks, however, in the plagiogranites (M)-like lower Sr isotope ratios and negative Eu anomalies are more abundant (Fig. 3a–f). Epidote-quartz veins (Fig. 3g), sharply crosscutting plagiogranites and gabbros, are accompanied by a metasomatic front that emanates from the vein into the host rock causing a secondary epidotization alteration. Massive epidote from the host rock matrix is characterized by (M)-like Sr isotope ratios of 0.7039–0.7044; ratios in the vein are also mostly (M)-like, but some crystals yielded higher (H)-type and even (MS)-type values (Fig. 3h). REE patterns of the vein epidote corresponds to (M)- and (MS)-like patterns of epidote found in basalts, epidosites and plagiogranites (Fig. 3i).

Discussion

The large range in whole-rock Sr isotope ratios previously measured in the extrusive suite of Troodos[29,34], 0.703 to 0.707, was interpreted to represent variable degrees of low-temperature alteration resulting in mixing between fresh MORB glass, $^{87}Sr/^{86}Sr = 0.7030$, and Sr derived from Cretaceous seawater[35], 0.7073 (Fig. 4). Nonetheless, going deeper in the crust into epidosites of the sheeted diabase dyke layer, this range significantly narrows down to 0.7050–0.7055. These relatively uniform whole rock values were attributed to interaction with an average Troodos hydrothermal fluid—a seawater-derived fluid, buffered by the mafic crust at the recharge zones of the hydrothermal cell[29]. The $^{87}Sr/^{86}Sr$ values in bulk epidote from epidosites measured in the

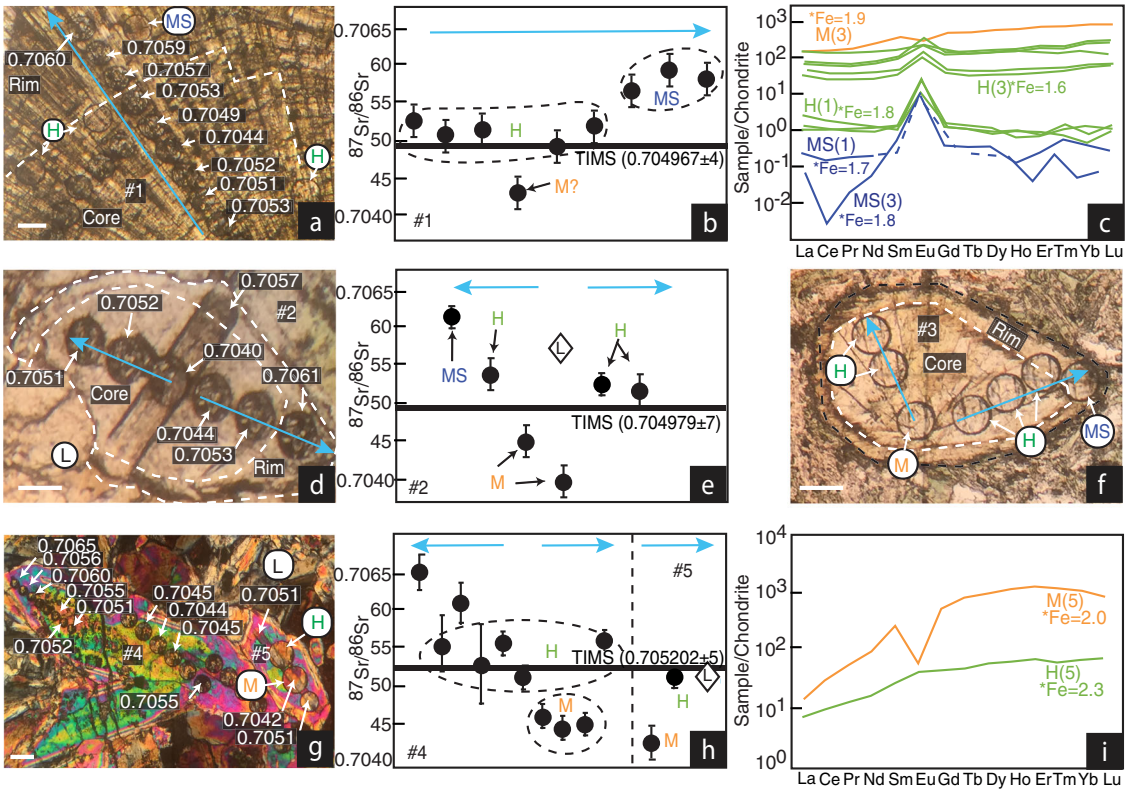

Fig. 2 Photomicrographs, $^{87}Sr/^{86}Sr$ isotope ratio profiles and chondrite-normalized REE patterns of zoned epidote crystals from basalt and epidosite. Crystal photomicrographs, $^{87}Sr/^{86}Sr$ values and corresponding REE patterns are indicated according to a particular numbered crystal (#1-5). Blue arrows indicate analyses direction. Horizontal black lines indicate $^{87}Sr/^{86}Sr$ of bulk epidote. $^{87}Sr/^{86}Sr$ values on the vertical axes are shown at the 3rd decimal place. **a** Plane-polarized light (PPL) image of epidote in amygdular basalt (AP-4). **b** $^{87}Sr/^{86}Sr$ values are spatially correlated to H- & MS- type REE patterns measured. **c** REE patterns measured in core and rim regions of crystals #1 and #3. **d** PPL image of radially grown epidote from amygdular basalt (Py-6). **e** $^{87}Sr/^{86}Sr$ values of crystal #2 are correlated to M-, H- & MS- type REE patterns measured in core to rim regions of texturally similar crystal #3, grown in an adjacent amygdule. **f** REE patterns measured in core to rim regions of crystal #3 are given in **c**. **g** Crossed-polarized light (XPL) image of euhedral epidote crystals (#4 & #5) in epidosite (CH-2E). $^{87}Sr/^{86}Sr$ values from crystal #5 are from ablation line L. **h** $^{87}Sr/^{86}Sr$ values of crystal #4 are correlated to M- & H- type REE patterns measured in core and rim regions of adjacent crystal #5. $^{87}Sr/^{86}Sr$ values from crystal #5 are spatially correlated to M- & H-type REE patterns measured over line L. **i** REE patterns of resorbed core and overgrown rim measured in crystal #5. Scale bars are 100 µm; Error bars are standard-error (SE); (M) Magmatic; (H) Hydrothermal; (MS) Modified Seawater; *Fe=Al/Fe molar ratio.

present study (blue diamonds in Fig. 4) are also consistent with precipitation from the average Troodos fluid, but the in-situ measurements (orange diamonds) show considerable $^{87}Sr/^{86}Sr$ zoning in single epidote crystals (0.704–0.7065) (sample CH-2E, Fig. 4) and indicate that no single fluid could have formed the Troodos epidosites.

Whole-rock and bulk epidote measurements tend to average out chemical and isotope zoning and thus cannot detect the origin or temporal variation of epidosite-forming fluids. The draw-back of bulk-rock analyses averaging grain-scale information is also known from other isotope studies of water-rock interaction. For example, in-situ measurements of oxygen isotope heterogeneities between grain centers and boundaries of high-grade metamorphic calcite from Naxos, Greece, have been shown to be averaged out by whole-rock powder analysis[36], thus concealing distinctive late meteoric fluids and their pathways along cracks and grain boundaries. The chromatographic continuum model previously suggested to account for gradual whole rock isotope evolution towards that of an incoming fluid[37] may be useful for a single episode of infiltration of a homogenous fluid. However, in complex cases where several generations of fluid infiltration are indicated by in-situ analysis, for example in Naxos marbles[37] and the Troodos ophiolite[29], the model is not compatible, and instead higher resolution grain-scale profiles should be used.

In general, REE patterns of epidotes from worldwide magmatic and metamorphic rocks display flat to LREE-enriched patterns[38]. However, REE patterns of epidote from metasomatic environments, like amygdules, miarolites and veins, are extremely variable[39]. Diverse REE patterns have been previously recorded in hydrothermal epidote from Troodos (Fig. 5a): (1) whole-grain groundmass-replacing epidote from greenschist facies diabase has flat patterns that are parallel to fresh-rock patterns, albeit with enriched absolute-REE contents[40]; (2) epidote vug-precipitates show LREE-enrichment, a positive Eu anomaly and flat HREE[40] (Fig. 5a); REE patterns (and $^{87}Sr/^{86}Sr$) of vug-epidote thus resemble those of modern hydrothermal vent fluids (Fig. 5b); (3) in situ analysis of miarolite-epidote cores display HREE-enrichment with negative Eu-anomalies resembling the REE pattern of the whole-rock host plagiogranite[28]. These epidote cores may be interpreted as precipitates of an exsolved magmatic fluid. The high temperatures and carrier ligand concentrations characteristic of magmatic fluids are expected to enable transportation of at least ppm-level REE contents[41] and up to 1300ppm in some cases[42], thus providing a source for REE-bearing precipitates.

REE patterns of several source fluids that may have been involved in epidote-precipitation are given in Fig. 5b. The granophyre and aplite REE patterns, determined by crush-leach extraction analysis of quartz-hosted fluid inclusions in felsic rocks, are LREE enriched and have negative Eu anomalies[42]. These may

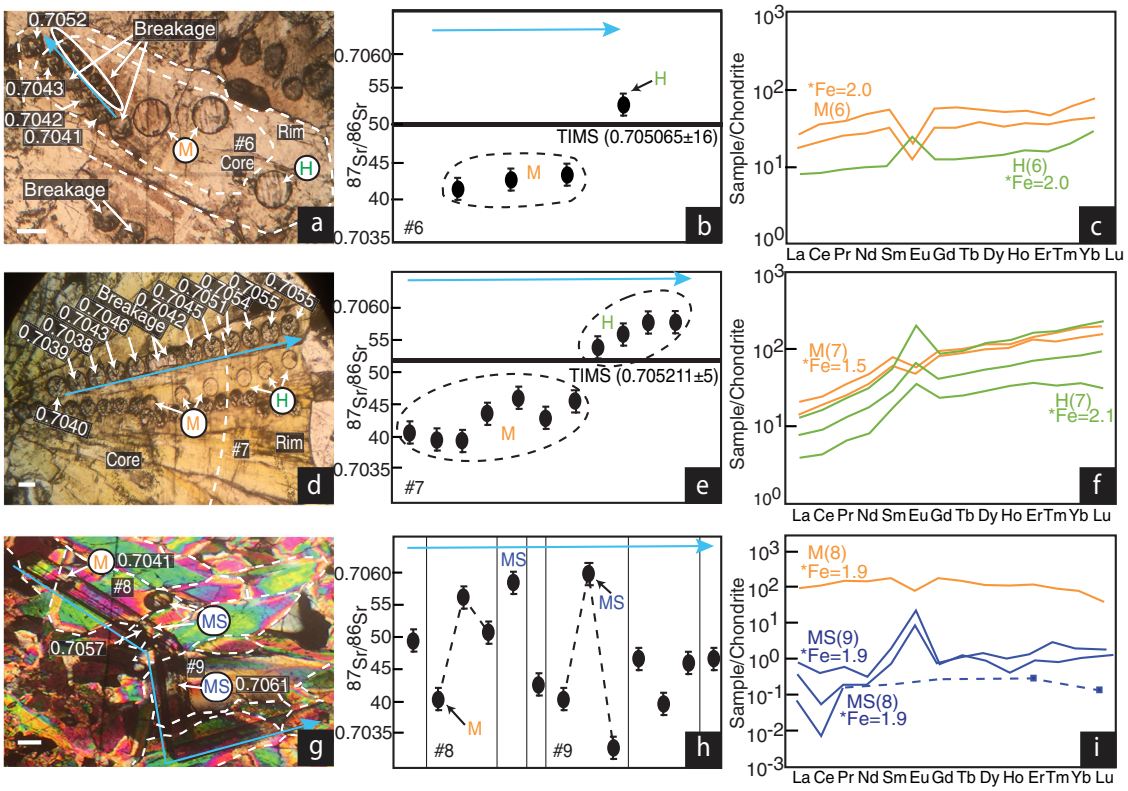

Fig. 3 Photomicrographs, $^{87}Sr/^{86}Sr$ isotope ratio profiles and chondrite-normalized REE patterns of zoned epidote crystals from plagiogranite. Crystal photomicrographs, $^{87}Sr/^{86}Sr$ values and corresponding REE patterns are indicated according to a particular numbered crystal (#6–9). Blue arrows indicate analyses direction. Horizontal black lines indicate $^{87}Sr/^{86}Sr$ of bulk epidote. $^{87}Sr/^{86}Sr$ values on the vertical axes are shown at the 3rd decimal place. **a** PPL image of epidote crystal #6 from epidotized plagiogranite SPL-2. **b**, **c** $^{87}Sr/^{86}Sr$ values are correlated to REE patterns in the corresponding regions. **d** PPL image of radially grown epidote crystal #7 in plagiogranite miarolite (PT-4); $^{87}Sr/^{86}Sr$ and REE ablation pits traverse the core to rim regions. **e**, **f** $^{87}Sr/^{86}Sr$ values are correlated to REE patterns measured in the core and rim regions. **g** XPL image of epidote vein cross-cutting a plagiogranite. **h**, **i** $^{87}Sr/^{86}Sr$ values of time-resolved ablation line across multiple crystals are correlated to M- & MS-type REE patterns measured in epidote crystals #8 and #9 in vein. Scale bars are 100 μm; Error bars are SE standard-error, M magmatic, H hydrothermal, MS modified seawater, *Fe = Al/Fe molar ratio.

be representative of early, Eu-depleted, magmatic-derived fluids and resemble (M)- type patterns in epidote. The Pacmanus and Vienna Woods vent fluids from modern BAB hydrothermal systems[9], used as analogs for ancient vent fluids, resemble the patterns of (H) domains albeit with slightly increased LREE ≥ HREE. Finally, the pattern of modern seawater[9], used as an analog for Cretaceous seawater, closely resembles the (MS)-type patterns with low REE contents and negative Ce anomalies; although in seawater positive Eu anomaly is absent.

Our in-situ analyses show that regardless of crustal depth, host rock type, and textural context, epidote growth domains can be classified by their coupled REE-Sr isotope characteristics into three major types: M- H- and MS-type fluid sources (Figs. 4, 5). Miarolites are cavities forming during the late stages of granite magma crystallization, often trapping exsolved magmatic fluids. Expectedly, the cores of miarolitic epidote from our study are characterized by REE patterns, which are similar to those measured in plagiogranites (Figs. 3f, 5a) and their Sr isotope ratios, 0.703–0.704, coincide with the whole rock values of fresh gabbros in Troodos[29] (Fig. 4). On the other edge of the fluid spectrum, the MS-type domains, which mostly occur at epidote rims, are most likely precipitated from seawater, as indicated by their negative Ce anomaly. However, the positive Eu anomaly coupled with Sr isotope ratios of ~0.706 suggest some modification of seawater by low water/rock ratio interaction with the mafic crust prior to epidote precipitation.

The most dominant fluid recorded by epidote is H-type, which is intermediate in REE contents and Sr isotope ratios with respect to the M-and MS-type fluids, and unanimously has a positive Eu anomaly. There are three possible scenarios that may account for the origin of H-type fluids. (1) The zoning of miarolite epidote from M- to H-type in REE patterns may record the evolution of magmatic fluids in a closed system[28], however since the Sr isotope ratio is significantly higher at the epidote rim, reaching 0.7052 (Fig. 3b), mixing of the magmatic fluid with an external one is more probable. (2) Mixing of magmatic water (M-type) and seawater (MS-type) at approximately equal amounts will produce the measured H-type REE-Sr values. (3) Seawater infiltration through the recharge zones involving prolonged interaction with diabase may result in averaging the Sr isotope ratio between Cretaceous seawater (0.7073) and mafic crust (0.703), forming an average Troodos hydrothermal fluid[29]. It would also produce fluids with positive Eu anomalies due to albitization of plagioclase. H-type domains have this characteristic REE-Sr coupling (Fig. 2, 3)), and may thus represent this large-scale rock-buffered seawater circulation. It follows that three distinct types of fluids sequentially flowed through the Troodos hydrothermal cell.

While epidosites are rarely found in modern oceanic crust[43], a bevy of epidosite alteration is recorded in Cretaceous ophiolites[44] (e.g. Troodos and Oman). It has been suggested that the higher Ca/Mg ratios[45] and fluid fluxes[29] of Cretaceous seawater infiltrating ocean crust may be necessary for epidotization to occur. However, the coupled Sr-isotope-REE zonation in Troodos epidotes indicates that no single fluid, regardless of its chemical composition, could have formed the epidosites. Field relations

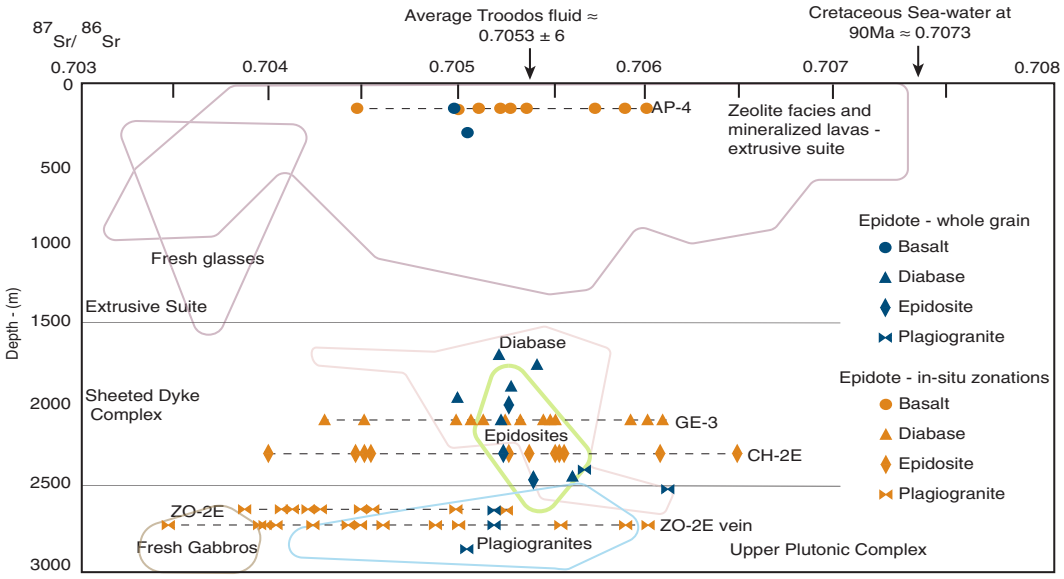

Fig. 4 Whole rock, bulk epidote and in-situ epidote $^{87}Sr/^{86}Sr$ values throughout the Troodos crustal section. $^{87}Sr/^{86}Sr$ values of epidote separates (blue symbols) and epidote domains (orange symbols) measured in the present study overlay outlined previous whole-rock $^{87}Sr/^{86}Sr$ ranges[29]. Dashed lines link ratios measured in individual domains of single zoned epidote grains (orange symbols); Sr isotope ratios of epidote separates from the same samples are shown in blue.

suggest that epidosites form by overprinting of diabase that was previously altered to greenschist facies mineral assemblage[23]. More recently, some epidosites were shown to precipitate into a newly-formed porosity, interpreted to form by dissolution of primary magmatic diabase by black-smoker hydrothermal fluid[44]. Our study of the epidosite paragenesis show that M-type epidote cores, precipitated by magmatic fluids, are truncated and later overgrown by euhedral rims precipitated by H-type fluids (Fig. 2g–i). Thus, irrespective of whether the initial rock was a primary mafic diabase or greenschist-facies assemblage, the introduction of acidic magmatic fluids (M-type), like those found venting at modern supra-subduction spreading environments[9], was necessarily part of the epidotization. Eventually, a dissipation of the magmatic fluid led to the influx of H-type fluid, partial resorption of the core due to disequilibrium and precipitation of euhedral H-type rims into the newly-formed porosity. While this may be the major mode of epidotization, some epidote crystals bear M-type characteristics throughout their growth. These may indicate regions in the dyke where permeability was low.

The consensus model for hydrothermal circulation in oceanic spreading centers involves deeply penetrating seawater interacting with diabase to obtain near magmatic Sr isotope ratios[29]. Upon fluid ejection through the upflow zones, the forming epidosites are supposed to inherit the near magmatic-like leached diabase isotope signature (Fig. 6, point 1). This is not likely the case as seen in Troodos, also applicable to other worldwide epidosite-bearing ocean crust sections, because (a) seawater-derived fluids cannot drive the immense mass transfer that is necessary to form intensive epidosite alteration. This may be the reason for the lack of documented epidosites from modern mid-ocean ridges. However, ingassing of hard mineral acids, such as HCL and H_2SO_4, found venting at modern supra-subduction environments, may destabilize chlorite, actinolite, and albite and leach Mg from the rocks[26]. (b) domains of zoned epidote crystals in epidosites, but also at shallower and deeper levels of the crust, are characterized by coupled REE—Sr isotope signatures indicative of sequential precipitation from magmatic, hydrothermal and modified seawater fluids. Moreover, the abundant domains with H-type intermediate Sr isotope ratio of ~0.705 are not necessarily derived from diabase-buffered fluid, but may have precipitated from a mixed seawater-magmatic fluid (Fig. 6, point 2, 3). The occurrence of M-type domains in epidote from the VMS deposits suggest mixing of the magmatic fluids with the H- and MS-type fluids may have been limited at times (Fig. 6, point 4). This process involves magmatic fluids episodically flooding the seawater-derived hydrothermal cell circulating through the upper crust. A possible mechanism for the pulsating magmatic fluid supply is volatile pressure build-up eventually leading to breach of the magma chamber, as commonly invoked to explain massive volatile degassing in oceanic dyke injection[46] and terrestrial volcanoes prior to eruption (Fig. 6, point 3). While episodic pulses of magmatic volatiles prevail, some epidote domains, even in deep-seated rocks, i.e. epidosites and plagiogranite, were precipitated from slightly modified seawater. This requires minimum interaction with rocks and thus rapid draw-down of seawater to ~2 km depth in the crust. Such intense downward seawater flow may be localized along steep normal faults during episodes of waning magmatic activity (Fig. 6, point 2).

With this model we suggest there were at least three types of fluids in circulation feeding the on-axis hydrothermal system of the Troodos oceanic crust—a modified seawater-derived fluid (MS-type), a magmatic fluid (M-type) and, a hydrothermal fluid (H-type)—possibly composed of the M- and MS-types, but most likely a seawater-derived rock-buffered fluid. The sequential M- to H-type zonation in epidote from the upflow zones (epidosites) suggests, magmatic fluids episodically flush the hydrothermal system, which is later dominated by a H-type fluid.

Methods

TIMS—whole grain strontium isotope ratio. For strontium isotope measurements, epidote separates (1.1 to 3.5 mg) were brought into solution by two consecutive steps. At first, the separates were digested in 0.5 ml of a mixture of concentrated HF and HNO_3 (5:1) and were placed on a hot plate for 42 h at 140 °C. Secondly, the solutions were dried at 95 °C and the residuum were re-dissolved in 1 ml 7 M HNO_3, placed on the hot plate for 24 hours, and afterwards dried at 90 °C. Strontium was purified by using 70 µl Sr. spec™ resin in miniaturized columns[47]. The samples were digested in 0.5 ml 2 M HNO_3 and loaded on the columns in 100 µl steps. Following, unwanted elements were removed by adding 1.2 ml of 2 M HNO_3 in 100 µl steps, 1 ml 7 M HNO_3 in 500 µl steps and 0.3 ml 2 M

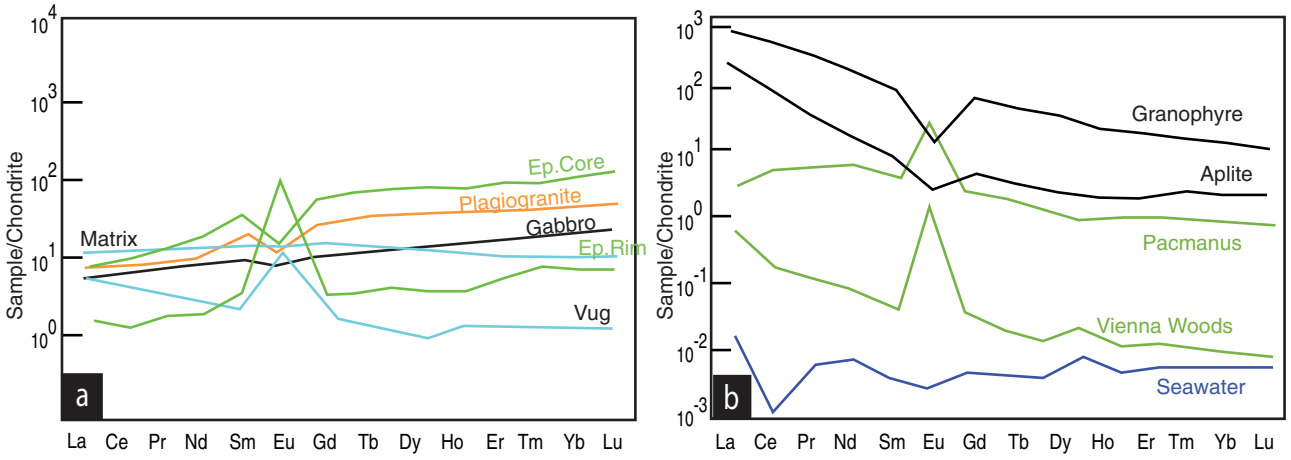

Fig. 5 REE patterns of rocks and fluids used for comparison with the epidote REE patterns measured in the present study. a Whole rock plagiogranite[28] (orange line) and gabbro[52] (black line) from the Troodos ophiolite; whole grain epidote from greenschist facies diabase[40] (light blue line), in-situ core and rim patterns of miarolite-epidote in plagiogranite[28] (green line). **b** Hydrothermal fluids venting in modern BAB[11] (green line), modern seawater[11] (blue line) and magmatic fluid inclusions from felsic rocks[42] (black line).

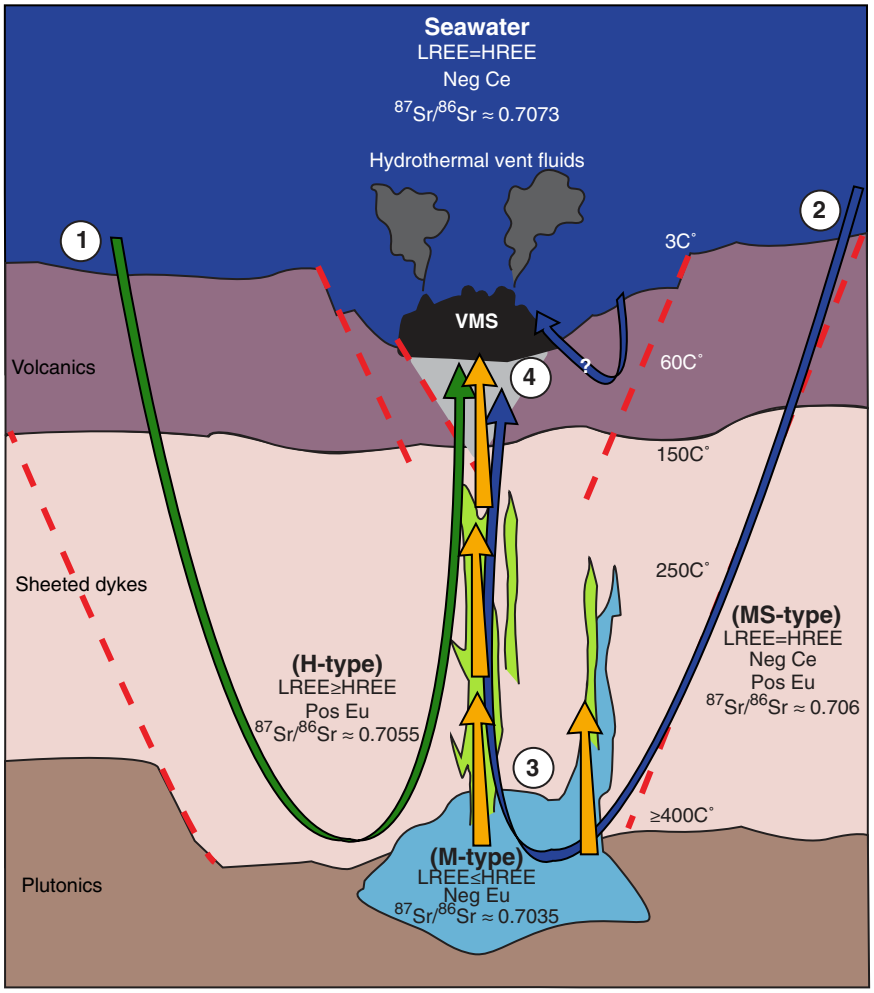

Fig. 6 Model of the on-axis hydrothermal system and the chemical characteristics of the fluid endmembers. (1) seawater infiltrates the crust evolving to H-type fluid (green arrow), and is recirculated through upflow zones, while leaching metals from the sheeted diabase dikes supplying metals to VMS deposits. (2) seawater is drawn down conjugate fault planes along the axis, quick enough to retain a slightly modified seawater $^{87}Sr/^{86}Sr$ and REE signature (MS-type, blue arrow). (3) emplaced plagiogranites exsolve magmatic volatiles (M-type, orange arrow), which flood the overlying hydrothermal system (H-type). MS-type and M-type fluids are funneled upwards in upflow zones, creating epidosite pipes. The precipitating epidote sequesters highly variable $^{87}Sr/^{86}Sr$ and REE values, pending on the most dominant fluid fluxing through the system at that particular time. (4) the fluid end-members are still partially unmixed even in the upper basalts hosting the VMS deposits. Model not to scale. Lithology color based on Fig. 1.

HNO_3 in 100 µl steps. Next, strontium was collected by adding 1 ml 0.05 M HNO_3 in 200 µl steps. The extracted solution was charged with 30 µl 0.1 M H_3PO_4 and evaporated to dryness. Organic material was removed by adding 40 µl of concentrated HNO_3, followed by drying and adding 40 µl H_2O_2 and drying. Strontium isotope measurements were performed by using a Thermo Scientific TRITON Plus thermal ionization mass spectrometer (TIMS) at the Isotope Geochemistry Laboratory at the MARUM—Centre for Marine Environmental Sciences, University of Bremen, Germany. For measurements, a rhenium filament was loaded with 1.5 µl Ta-emitter, and then loaded with the sample digested in 2 µl 0.1 M H_3PO_4 and conditioned by heating until red heat occurred. The instrumental fractionation was corrected to the natural $^{88}Sr/^{86}Sr$ ratio of 0.1194. The blank contamination (<50 pg Sr) was negligible in comparison to the Sr concentrations of the samples loaded on the filament (>200 ng Sr). The accuracy relative to the reference material NIST SRM 987 was 0.710243 ± 0.00006 (2sd, $n = 2$). The long-term reproducibility of NIST SRM 987 (from December 2011 to February 2017) was 0.710249 ± 0.000024 (2sd, $n = 231$).

LA-ICP-MS—in-situ trace element contents. The determination of trace element concentrations from thin sections was performed by using a Thermo-Scientific Element 2 inductively coupled plasma—mass spectrometer (ICP-MS) coupled to a NewWave UP193 laser ablation system at the Faculty of Geosciences, University of Bremen. The irradiance for ablation was set to 1 GW/cm^2 and for spot measurements the beam diameter was set to between 75 µm and 50 µm depending on sample size. Pulse rates of 5 Hz were used. The carrier gas was helium and argon was added as make-up gas, both with 0.8 l/min. NIST 610 was used as the external calibration standard and Ca as the internal standard previously measured by EMPA. The computation of the trace element concentrations was performed with the Cetac GeoPro^{TM} software. The reference materials BCR-2G and BHVO-2G were measured at least every 20 measurements to ensure the analytical precision and accuracy. The relative standard deviation (RSD) of the reference material was used as an indicator for precision.

LA-MC-ICP-MS—in-situ strontium isotope ratio. Epidote crystals were polished, imaged and analyzed either in-situ in petrographic thin sections or as separated grains mounted in 1-inch epoxy rounds. $^{87}Sr/^{86}Sr$ isotope ratios of epidote were measured at the University of California, Davis Interdisciplinary Center for Plasma Mass Spectrometry. For the Sr isotope analyses a Nd:YAG 213 nm laser (New Wave Research UP213) was coupled to a Nu Plasma HR MC-ICP-MS (Nu032). Core to rim Sr isotope traverses across epidote were analyzed by using 10-Hz laser pulses with 4–7 J/cm^2 photon intensities and 25 s dwell times, forming 65–100 µm diameter pits. The $^{87}Sr/^{86}Sr$ isotope ratio was normalized for instrumental mass discrimination by monitoring the $^{86}Sr/^{88}Sr$ isotope ratio ($^{86}Sr/^{88}Sr = 0.1194$), and ^{87}Rb interference was corrected by monitoring the ^{85}Rb signal, assuming the same mass bias coefficient as Sr (calculated from the 86/88 ratio) and an $^{87}Rb/^{85}Rb$ ratio of 0.3856. Krypton interference, originating from the argon supply, was subtracted using the on peak zero method before each analysis. Accuracy and reproducibility of the LA-MC-ICP-MS analysis were evaluated using an in-house isotopic reference material, a marine aragonite otolith (ear stone) from a White Seabass (*Atractoscion nobilis*) named SBO, collected offshore Baja California. Replicate analyses for the otolith yielded a mean $^{87}Sr/^{86}Sr$ isotope ratio of 0.70916 ± 0.00013 ($n = 70$, ±2σ) This value is in good agreement with the global average $^{87}Sr/^{86}Sr$ isotope value of modern seawater, 0.70918[48], and compares well to values previously produced in this laboratory[48–50]. MPI DING iRM StHs6/80-G (St. Helens Andesitic Ash Glass) and in-house White Sturgeon (Acipenser transmontanus) pectoral fin ray named 'SSFR' (from Sterling Caviar Aqua Farm, CA, USA) were also measured in this study. StHs6/80-G was used to evaluate potential polyatomic spectral interferences (predominately CaCa+ and FeSi+) and doubly-charged REE spectral interferences (Er^{2+}, Yb^{2+}, Lu^{2+} and Hf^{+2}). SSFR was used to evaluate the accuracy threshold of the Rb correction because of its similar Rb/Sr ratio to the epidote grains (raw $^{85}Rb/^{88}Sr$ ~ 0.003). These iRMs yielded $^{87}Sr/^{86}Sr$ means of 0.70471 ± 0.00144 ($n = 16$, ±2σ) and 0.70570 ± 0.00019 ($n = 9$, ±2σ) respectively, both within measurement error of accepted values (0.703497 ± 0.000035[51], and 0.70575 ± 0.0001, in-house average). StHs6/80-G yielded a heavy $^{87}Sr/^{86}Sr$ value and greater measurement error due to its abundant rubidium content (Rb/Sr = 0.06[51]), which is significantly greater than Rb/Sr in the epidote samples.

We carried out our Sr isotope analyses using enhanced mass resolving power >7000 (source slit set to 0.05 mm and alfa slits engaged, each with 25% signal reduction) to attenuate potential spectral interferences from REE doubly-charged species (e.g., $^{174}Yb^{2+}$) and molecular species (i.e., CaCa+ and FeSi+) endemic in epidote sample matrices. $^{56}Fe^{28}Si^+$ was monitored with 84/88 ratios in StHs6/80-G and epidote grains with no significant effect. This was measured directly in StHs6/80-G average raw 84/88 = 0.0063 ± 0.0001 ($n = 16$, ±2σ) compared to White Seabass average raw 84/88 = 0.0065 ± 0.0001 ($n = 70$, ±2σ). Note that it is not possible to spectrally resolve $FeSi^+$ species using the mass resolution capabilities of the Nu Plasma HR instrument. However, increasing resolving power does effectively reduce the transmission of the FeSi+ species to below the threshold of the faraday detectors. These signals were not observed. Alternatively, it may be possible that these molecular species do not abundantly form and transmit with laser ablation coupled with hot-plasma sample introduction (RF power = 1300). Increasing the mass resolving power was determined the most accurate and robust method for epidote samples considering their range in REE, Sr and Ca composition. LA-MC-ICP-MS data were initially reduced offline using a custom Microsoft Excel spreadsheet. A five-point moving average was applied to reduce the noise typically associated with LA data. A data time window, visualized as a peak in the Sr signal above background measurements, was selected and the average of all the $^{87}Sr/^{86}Sr$ ratios within that time window were averaged with 2SE outlier removal. Standard error of the mean is used to report the precision of individual $^{87}Sr/^{86}Sr$ analyses.

Data availability

All data generated during the study, including in-situ REE contents and both in-situ and whole grain Sr isotope ratios, are available in supplementary information file (Supplementary Data 1). While, Fig. 2, 3 shows spatially correlated REE-Sr data in epidote, there are cases where this effort was not possible, e.g., fine-grained epidote. As such, there are instances of either REE patterns or Sr isotope data for an individual rock/crystal. However, in these cases, the distinctive REE patterns or Sr isotope fluid signatures, discussed in the main text, are still represented. Data can be found on Pangaea.de repository under the title 'In-situ REE patterns and Sr isotope ratios of zoned Epidote minerals'.

Received: 27 March 2020; Accepted: 21 October 2020;
Published online: 25 November 2020

References

1. Edmond, J. M. et al. On the formation of metal-rich deposits at ridge crests. *Earth Planet. Sci. Lett.* **46**, 19–30 (1979).
2. Scott, S. D. Submarine hydrothermal systems and deposits. In *Geochemistry of Hydrothermal Ore Deposits*, 797–875 (John Wiley & Sons, Hoboken NJ, 1997).
3. Von Damm, K. L. Seafloor hydrothermal activity: black smoker chemistry and chimneys. *Annu. Rev. Earth Planet. Sci.* **18**, 173–204 (1990).
4. Cann, J. & Gillis, K. Hydrothermal insights from the Troodos ophiolite, Cyprus. In *Hydrogeology of the Oceanic Lithosphere*, 272–310 (Cambridge Univ. Press, Cambridge, 2004).
5. Jowitt, S. M., Jenkin, G. R., Coogan, L. A. & Naden, J. Quantifying the release of base metals from source rocks for volcanogenic massive sulfide deposits: Effects of protolith composition and alteration mineralogy. *J. Geochem. Exploration* **118**, 47–59 (2012).
6. Yang, K. & Scott, S. D. Magmatic fluids as a source of metals in seafloor hydrothermal systems. *Back-Arc Spreading Systems: Geological, Biological, Chemical, and Physical Interactions*, 163–184 (AGU Monograph, American Geophysical Union, Washington DC, 2006).
7. Langmuir, C. H., Bézos, S., Escrig, S. & Parman, S. W. Chemical systematics and hydrous melting of the mantle in back-arc basins. *Back-Arc Spreading Systems: Geological, Biological, Chemical, and Physical Interactions* (pp. 87–146. AGU Monograph, American Geophysical Union, Washington DC, 2006).
8. Klinkhammer, G. P., Elderfield, H., Edmond, J. M. & Mitra, A. Geochemical implications of rare earth element patterns in hydrothermal fluids from mid-ocean ridges. *Geochim. Cosmochim. Acta* **58**, 5105–5113 (1994).
9. Douville, E. et al. Yttrium and rare earth elements in fluids from various deep-sea hydrothermal systems. *Geochim. Cosmochim. Acta* **63**, 627–643 (1999).
10. Craddock, P. R. et al. Rare earth element abundances in hydrothermal fluids from the Manus Basin, Papua New Guinea: Indicators of sub-seafloor hydrothermal processes in back-arc basins. *Geochim. Cosmochim. Acta* **74**, 5494–5513 (2010).
11. Bach, W. et al. Controls of fluid chemistry and complexation on rare-earth element contents of anhydrite from the Pacmanus subseafloor hydrothermal system, Manus Basin, Papua New Guinea. *Mineral. Deposit* **38**, 916–935 (2003).
12. Reeves, E. P. et al. Geochemistry of hydrothermal fluids from the PACMANUS, Northeast Pual and Vienna Woods hydrothermal fields, Manus basin, Papua New Guinea. *Geochim. Cosmochim. Acta* **75**, 1088–1123 (2011).
13. Little, C. T., Cann, J. R., Herrington, R. J. & Morisseau, M. Late Cretaceous hydrothermal vent communities from the Troodos ophiolite, Cyprus. *Geology* **27**, 1027–1030 (1999).
14. Humphris, S. E. & Cann, J. R. Constraints on the energy and chemical balances of the modern TAG and ancient Cyprus seafloor sulfide deposits. *J. Geophys. Res.* **105**, 28477–28488 (2000).
15. Martin, A. J. et al. Effects of magmatic volatile influx in mafic VMS hydrothermal systems: evidence from the Troodos ophiolite, Cyprus. *Chem. Geol.* **531**, https://doi.org/10.1016/j.chemgeo.2019.119325 (2020).
16. Pearce, J. A. & Robinson, P. T. The Troodos ophiolitic complex probably formed in a subduction initiation, slab edge setting. *Gondwana Res.* **18**, 60–81 (2010).

17. Woelki, D., Regelous, M., Haase, K. M. & Beier, C. Geochemical mapping of a paleo-subduction zone beneath the Troodos Ophiolite. *Chem. Geol.* **523**, 1–8 (2019).
18. Morag, N. et al. The origin of plagiogranites: coupled SIMS O isotope ratios, U-Pb dating and trace element composition of zircon from the Troodos ophiolite, Cyprus. *J. Petrol.* **61**, https://doi.org/10.1093/petrology/egaa057 (2020).
19. Mukasa, S. B. & Ludden, J. N. Uranium-lead isotopic ages of plagiogranites from the Troodos ophiolite, Cyprus, and their tectonic significance. *Geology* **15**, 825–828 (1987).
20. Richards, H. G., Cann, J. R. & Jensenius, J. Mineralogical zonation and metasomatism of the alteration pipes of Cyprus sulfide deposits. *Econ. Geol.* **84**, 91–115 (1989).
21. Schiffman, P., Smith, B. M., Varga, R. J. & Moores, E. M. Geometry, conditions and timing of off-axis hydrothermal metamorphism and ore-deposition in the Solea graben. *Nature* **325**, 423–425 (1987).
22. Alt, J. C. et al. Hydrothermal alteration of a section of upper oceanic crust in the Eastern Equatorial Pacific: a synthesis of results from site 504 (DSDP LEGS 69, 70, and 83, and ODP LEGS 111, 137, 140 and 148). In *Proceedings of the Ocean Drilling Program, scientific results* **148**, 417–434 (1996).
23. Richardson, C. J., Cann, J. R., Richards, H. G. & Cowan, J. G. Metal-depleted root zones of the Troodos ore-forming hydrothermal systems, Cyprus. *Earth Planet. Sci. Lett.* **84**, 243–253 (1987).
24. Coleman, R. G. *Ophiolites: Ancient Oceanic Lithosphere?* (Springer-Verlag, Berlin, 1977).
25. Seyfried, W. E., Berndt, M. E. & Seewald, J. S. Hydrothermal alteration processes at midocean ridges: constraints from diabase alteration experiments, hot-spring fluids, and composition of the oceanic crust. *The Canadian Mineralogist* **26**, 787–804 (1988).
26. Bach, W., Jöns, N. & Klein, F. Metasomatism within the ocean crust. *Metasomatism and the Chemical Transformation of Rock* (pp. 253–288. Springer, Berlin-Heidelberg, 2013).
27. Kelley, D. S., Robinson, P. T. & Malpas, J. G. Processes of brine generation and circulation in the oceanic crust: fluid inclusion evidence from the Troodos ophiolite, Cyprus. *J. Geophys. Res.* **97**, 9307–9322 (1992).
28. Anenburg, M., Katzir, Y., Rhede, D., Jöns, N. & Bach, W. Rare earth element evolution and migration in plagiogranites: a record preserved in epidote and allanite of the Troodos ophiolite. *Contributions Mineral. Petrol.* **169**, 25 (2015).
29. Bickle, M. J. & Teagle, D. A. Strontium alteration in the Troodos ophiolite: implications for fluid fluxes and geochemical transport in mid-ocean ridge hydrothermal systems. *Earth Planet. Sci. Lett.* **113**, 219–237 (1992).
30. Gillis, K. M. The rootzone of an ancient hydrothermal system exposed in the Troodos ophiolite, Cyprus. *J. Geol.* **110**, 57–74 (2002).
31. Gillis, K. M. Subseafloor geology of hydrothermal root zones at oceanic spreading centers. *Energy and Mass Transfer in Marine Hydrothermal Systems*, pp. 53-69 (Dahlem Univ. Press, Berlin, 2003).
32. Patten, C. G., Pitcairn, I. K. & Teagle, D. A. H. Hydrothermal mobilization of Au and other metals in supra-subduction oceanic crust: Insights from the Troodos ophiolite. *Ore Geol. Rev.* **86**, 487–508 (2017).
33. Bird, D. K. & Spieler, A. R. Epidote in geothermal systems. *Rev. Mineral. Geochem.* **56**, 235–300 (2004).
34. Chapman, H. J. & Spooner, E. T. C. 87Sr enrichment of ophiolitic sulphide deposits in Cyprus confirms ore formation by circulating seawater. *Earth Planet. Sci. Lett.* **35**, 71–78 (1977).
35. Burke, W. H. et al. Variation of seawater $^{87}Sr/^{86}Sr$ throughout Phanerozoic time. *Geology* **10**, 516–519 (1982).
36. Lewis, S., Holness, M. & Graham, C. Ion microprobe study of marble from Naxos, Greece: Grain-scale fluid pathways and stable isotope equilibration during metamorphism. *Geology* **26**, 935–938 (1998).
37. Bickle, M. J. & Baker., J. Advective-diffusive transport of isotopic fronts: an example from Naxos, Greece. *Earth Planet. Sci. Lett.* **97**, 78–93 (1990).
38. Frei, D., Liebscher, A., Wittenberg, A. & Shaw, C. S. J. Crystal chemical controls on rare earth element partitioning between epidote-group minerals and melts: an experimental and theoretical study. *Contributions Mineral. Petrol.* **146**, 192–204 (2003).
39. Frei, D., Liebscher, A., Franz, G. & Dulski, P. Trace element geochemistry of epidote minerals. *Rev. Mineral. Geochem.* **56**, 553–605 (2004).
40. Gillis, K. M., Ludden, J. N. & Smith, A. D. Mobilization of REE during crustal aging in the Troodos Ophiolite, Cyprus. *Chem. Geol.* **98**, 71–86 (1992).
41. Debruyne, D., Hulsbosch, N. & Muchez, P. Unraveling rare earth element signatures in hydrothermal carbonate minerals using a source–sink system. *Ore Geol. Rev.* **72**, 232–252 (2016).
42. Banks, D. A., Yardley, B. W. D., Campbell, A. R. & Jarvis, K. E. REE composition of an aqueous magmatic fluid: a fluid inclusion study from the Capitan Pluton, New Mexico, USA. *Chem. Geol.* **113**, 259–272 (1994).
43. Banerjee, N. R., Gillis, K. M. & Muehlenbachs, K. Discovery of epidosites in a modern oceanic setting, the Tonga forearc. *Geology* **28**, 151–154 (2000).
44. Cann, J., McCaig, A. M. & Yardley, B. W. D. Rapid generation of reaction permeability in the roots of black smoker systems, Troodos ophiolite, Cyprus. *Geofluids* **15**, 179–192 (2015).
45. Coggon, R. M., Teagle, D. A., Smith-Duque, C. E., Alt, J. C. & Cooper, M. J. Reconstructing past seawater Mg/Ca and Sr/Ca from mid-ocean ridge flank calcium carbonate veins. *Science* **327**, 1114–1117 (2010).
46. Gillis, K. M. & Roberts, M. D. Cracking at the magma–hydrothermal transition: evidence from the Troodos Ophiolite, Cyprus. *Earth Planet. Sci. Lett.* **169**, 227–244 (1999).
47. Deniel, C. & Pin, C. Single-stage method for the simultaneous isolation of lead and strontium from silicate samples for isotopic measurements. *Anal. Chim. Acta* **426**, 95–103 (2001).
48. Willmes, M., Glessner, J. J. G., Carleton, S. A., Gerrity, P. C. & Hobbs, J. A. $^{87}Sr/^{86}Sr$ isotope ratio analysis by laser ablation MC-ICP-MS in scales, spines, and fin rays as a non-lethal alternative to otoliths for reconstructing fish life history. *Canadian J. Fish. Aqunkatic Sci.* **73**, 1852–1860 (2016).
49. Sellheim, K. et al. Validating fin ray microchemistry as a tool to reconstruct the migratory history of White Sturgeon. *Trans. Am. Fisheries Soc.* **146**, 844–857 (2017).
50. Phillis, C. C., Sturrock, A. M., Johnson, R. C. & Weber, P. K. Endangered winter-run Chinook salmon rely on diverse rearing habitats in a highly altered landscape. *Biol. Conserv.* **217**, 358–362 (2018).
51. Jochum, K. P. et al. GeoReM: a new geochemical database for reference materials and isotopic standards. *Geostandards Geoanal. Res.* **29**, 333–338 (2005).
52. Kay, R. W. & Senechal, R. G. The rare earth geochemistry of the Troodos ophiolite complex. *J Geophys. Res.* **81**, 964–970 (1976).

Acknowledgements

This study was funded by the German-Israeli Foundation for Scientific Research and Development grant #I-1357-301.8/2016 to W. Bach and Y. Katzir.

Author contributions

S.F. sampled and produced rock thin sections and mineral separates; conducted LA-ICP-MS, EMP and TIMS analyses; developed and completed the petrological study and wrote the manuscript. Y.K. co-generated the project, contributed to writing and editing the manuscript, co-organized and led the field work. W.B. co-generated the project, co-organized and led the field work, contributed to writing and editing the manuscript. L.S. participated in the field work, mentored and contributed to the TIMS sample preparation and analyses, contributed to writing and editing the manuscript. J.G. conducted the laser ablation MC-ICP-MS strontium isotopic composition analyses, contributed to writing and editing the manuscript.

Competing interests

The authors declare no competing interests.

Additional information

Supplementary information is available for this paper at https://doi.org/10.1038/s43247-020-00051-0.

Correspondence and requests for materials should be addressed to S.F.

Peer review information Primary handling editor: Joe Aslin.

Reprints and permission information is available at http://www.nature.com/reprints

Publisher's note Springer Nature remains neutral with regard to jurisdictional claims in published maps and institutional affiliations.